

Giant exchange bias in the single-layered Ruddlesden-Popper perovskite SrLaCo_{0.5}Mn_{0.5}O₄Ranjana R. Das,¹ Priyadarshini Parida,² A. K. Bera,³ Tapan Chatterji,⁴ B. R. K. Nanda,² and P. N. Santhosh^{1,*}¹*Low Temperature Physics Laboratory, Department of Physics, Indian Institute of Technology Madras, Chennai 600036, India*²*Condensed Matter Theory and Computational Laboratory, Department of Physics, Indian Institute of Technology Madras, Chennai 600036, India*³*Solid State Physics Division, Bhabha Atomic Research Centre, Mumbai 400085, India*⁴*Institut Laue-Langevin, 71 Avenue des Martyrs, 38000 Grenoble, France*

(Received 6 September 2018; revised manuscript received 16 October 2018; published 15 November 2018)

Exchange bias (EB) as large as ~ 5.5 kOe is observed in SrLaCo_{0.5}Mn_{0.5}O₄, which is the highest ever found in any layered transition-metal oxides including Ruddlesden-Popper series. Neutron-diffraction measurement rules out long-range magnetic ordering and together with dc magnetic measurements suggests formation of short-range magnetic domains. Ac magnetic susceptibility, magnetic memory effect, and magnetic training effect confirm the system to be a cluster spin glass. By carrying out density functional calculations on several model configurations, we propose that EB is originated at the boundary between Mn-rich antiferromagnetic and Co-rich ferromagnetic domains at the subnanoscale. Reversal of magnetization axis on the Co side alters the magnetic coupling between the interfacial Mn and Co spins, which leads to EB. Our analysis infers that the presence of competing magnetic interactions is sufficient to induce exchange bias and thereby a wide range of materials exhibiting giant EB can be engineered for designing novel magnetic memory devices.

DOI: [10.1103/PhysRevB.98.184417](https://doi.org/10.1103/PhysRevB.98.184417)**I. INTRODUCTION**

Complex three-dimensional (3D) perovskite oxides offer a rich materials platform for investigating emergent phenomena like ferromagnetic insulators [1], multiferroics [2–4], and colossal magnetoresistance [5,6] that arise due to a complex web of interactions involving spin, charge, orbital, and lattice degrees of freedom in the three-dimensional space [7]. In order to realize exotic quantum phenomena, a natural extension of this 3D cubic perovskite is to reduce the interaction dimensionality by either making artificial heterosuperlattices or tuning the stoichiometry so that the active layers involved in the coupling process are well separated [8–10]. While the former is sensitive to the growth condition, the latter is thermodynamically stable and can be synthesized under ambient conditions.

The layered Ruddlesden-Popper (RP) series with general formula (A)_{n+1}(B)_nO_{3n+1} [11] are among the most preferred materials to study the physics of reduced dimensionality as they exhibit interesting properties such as superconductivity [12,13], charge ordering (CO) or orbital ordering (OO) [14], ferroelectricity [15], and colossal magnetoresistance [16]. The crystal structure of $n = 1$ RP compounds, A'A(B/B')O₄, can be described by the periodic stacking of the layers with the order A/A'O|A/A'O|B/B'O₂ as shown in Fig. 1. The structure may also be described as magnetically active (A'/A)(B/B')O₃ perovskite blocks well separated by (A'/A)O layers along [001]. Under suitable conditions, the synthesis of these single-layer RP compounds will produce B and B' rich domains at the subnanoscale. The boundary separating these

domains can further constrain certain long-range magnetic order, and in turn novel quantum states can be formed which may not be observed in pristine perovskites ABO₃. While there is a large amount of literature available on single-layered RP compounds with one transition-metal element, very few works have reported the results with two transition-metal elements in a single-layered RP system [17–19]. Therefore, there is lack of evidence on emerging quantum states at the boundary of two different magnetic domains in these layered RP compounds.

In the present paper, we report a monolayered RP phase based layered perovskite oxide SrLaCo_{0.5}Mn_{0.5}O₄ (SLCMO) synthesized by sol-gel method. The dc and ac magnetic measurements along with the neutron powder-diffraction (NPD) measurements point to cluster spin-glass (CG) like magnetic behavior as well as a giant exchange bias (EB) effect. In fact the EB in this layered system shows fivefold increase compared to the EB reported in other layered oxide compounds such as single layer RP Sr_{0.5}Pr_{1.5}CoO₄ (1 kOe) [20], double layer RP Sr₃FeMoO₇ (0.2 kOe) [21], layered oxychalcogenides La₂O₃Mn₂Se₂ (0.5 kOe) [22], and double perovskites SrLaCoMnO₆ (0.3 kOe) [23]. The density functional calculations further confirm the existence of giant EB in this compound, and it is attributed to the anisotropic magnetic coupling among the Mn and Co spins.

II. EXPERIMENTAL SECTION**A. Synthesis details**

Despite remarkable electronic and magnetic properties, the synthesis of the phase pure stoichiometric single-layer RP system is quite challenging. The probability of obtaining a perovskite phase was often detected in the

*santhosh@iitm.ac.in

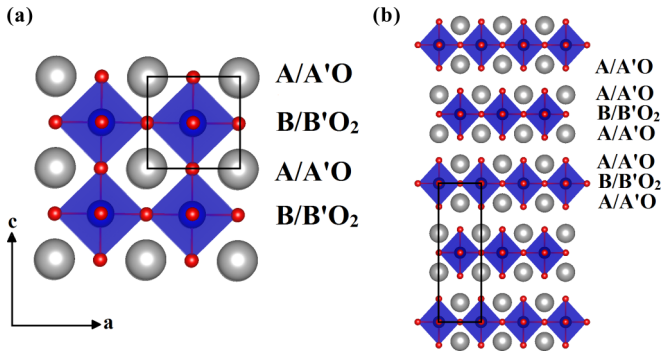


FIG. 1. (a) Ideal perovskite structure in which the alternate stacking of A/A'O and B/B'O₂ layers of the perovskite block is presented (the square indicates one unit cell of perovskite). (b) Single-layered Ruddlesden-Popper (RP) perovskite in which the adjacent perovskite block is replaced with a new order of the form A/A'O|A/A'O|B/B'O₂. The rectangle represents one unit cell of the RP tetragonal lattice.

polycrystalline sample, which was synthesized by solid-state synthesis methods [24]. Thus a citrate gel technique is used to prepare a polycrystalline sample of SLCMO. La₂O₃, Mn(CH₃COO)₂ · 4H₂O, Sr(NO₃)₂, and Co(NO₃)₂ · 6H₂O in stoichiometric amounts were first dissolved in dilute nitric acid (HNO₃), and then an excess of citric acid and ethylene glycol (CH₂OH)₂ were added. La₂O₃ was preheated at 1273 K before adding in dilute nitric acid. The dissolved solution was heated on a hot plate, resulting in the formation of a gel. The gel was dried at 523 K and then heated to 973 K for 12 h to remove the organic components and to decompose the nitrates. SLCMO ceramic was subsequently sintered at 1573 K for 36 h in air with intermittent grindings for homogeneity.

B. Characterization details

Laboratory x-ray powder-diffraction (XRPD) measurements were conducted at room temperature on a PANalytical X'pert using a Cu K α radiation source ($\lambda = 1.54056 \text{ \AA}$). The NPD patterns were recorded in zero field by using a high-resolution powder diffractometer SPODI at the research reactor FRM-II (Garching, Germany) with monochromatic neutrons of $1.5481(1) \text{ \AA}$ over the 2θ range of $6\text{--}150^\circ$ with a step size of 0.05° . X-ray photoelectron spectra (XPS) of SLCMO were recorded by an instrument with Mg-K α as the x-ray source, and a PHOIBOS 100MCD analyzer SPECS operated under ultrahigh vacuum (10^{-9} mbar). The XPS spectra were fitted by the CasaXPS software (Casa Software Ltd) using Gaussian-Lorentzian peak functions and Shirley background subtraction. Dc and ac magnetic susceptibility measurements were carried out in a commercial superconducting quantum interference device (VSM-SQUID) magnetometer 70 kOe (MPMS). Dc magnetization curves in zero-field cooled (ZFC) and field cooled (FC) cycles were performed at several magnetic fields. Both the ZFC and FC magnetization versus temperature (M - T) curves were measured during the warming process. Isothermal magnetization, M (H), hysteresis loops were measured under ZFC and FC conditions in the range $-70 \leq \mu_0 H \leq 70$ kOe at different temperatures. For the ZFC case, the samples were first cooled from 300 K down to the

temperature of measurement under zero magnetic field, and five-quadrant $M(H)$ measurements were performed starting at $H = 0$. For FC analysis, the samples were cooled each time under an applied magnetic field from 300 K down to measurement temperature.

C. Computational details

Pseudopotential based density functional calculations are carried out using the plane waves as basis sets as implemented in Quantum ESPRESSO [25]. We have used the generalized gradient approximation (GGA) exchange correlation functional, given by Perdew, Burke and Ernzerhof, incorporated with the Hubbard U correction to consider the strong correlation effect. We have taken $U = 5$ eV in our calculations. In all our calculations ultrasoft-type pseudopotentials are considered. The kinetic-energy cutoffs for the plane waves and charge densities are taken as 30 and 250 Ry, respectively. The k-mesh of $3 \times 9 \times 4$ with 30 irreducible k-points are used in the calculations.

III. EXPERIMENTAL RESULTS

A. Crystal structure

1. X-ray and neutron diffraction

The crystal structure of SLCMO is examined through XRPD and NPD measurements. NPD measurements are performed at various temperatures ranging from 300 to 4 K. The Rietveld refinement of NPD patterns collected at 300 and 4 K are shown in Fig. 2 and Rietveld refinement at 50 and 100 K can be seen in the Supplemental Material [26]. The data indicate that the compound crystallizes in a single-layered RP phase with the body-centered tetragonal lattice having space group $I4/mmm$ no. (139) and the schematic of this structure is presented in Fig. 1(b) (where A/A' = Sr/La as silver balls and B/B' = Co/Mn as blue balls and O as red balls). The room-temperature lattice parameters a and c are found to be $3.8420(1)$ and $12.6211(1) \text{ \AA}$, respectively, from the NPD. The lattice parameters a and c change by 0.23 and 0.17%, respectively, over the temperature range 4–300 K. Details of crystal structure parameters obtained from XRPD and NPD are provided in the Supplemental Material [26]. From the nuclear structure refinement, we conclude that SLCMO is stoichiometric. We observed a large difference between the equatorial and apical bonds of Mn/Co-O₆ octahedra with bond length 1.92 and 2.09 \AA , respectively, and the difference in bond length is close to 0.17 \AA . We note that Jahn-Teller active LaSrMnO₄ has a similar difference in the bond length [27]. The obtained bond lengths (Table S3 in the Supplemental Material [26]) from the NPD refinement signal the compression of equatorial and elongated apical bonds, indicating the presence of the Jahn-Teller active Mn³⁺ ion ($t_{2g}^3 e_g^1$).

In order to obtain insight into the oxidation states of the ions, we have performed bond-valence-sum (BVS) calculations from the refined atomic positions. The derived BVS values reveal a mixed valence state of both Co^{2+/3+} and Mn^{3+/4+} ions.

Temperature evolution of NPD shows that there is no structural change in the measured temperature range.

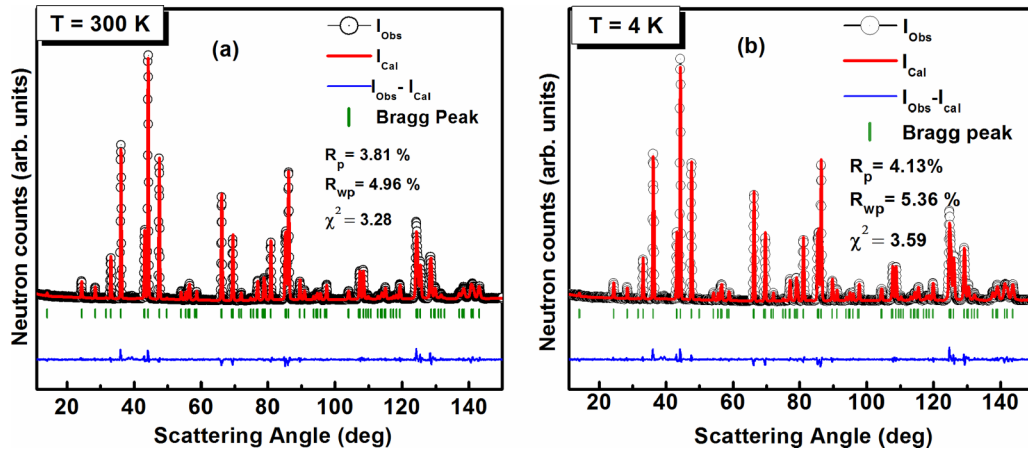


FIG. 2. Neutron powder-diffraction pattern of SrLaCo_{0.5}Mn_{0.5}O₄ measured at (a) 300 K and (b) 4 K. We excluded the 2θ region 38–40° of the neutron-diffraction patterns during Rietveld refinements, as it consists of two weak peaks from the sample holder.

Furthermore, no additional magnetic peak or increase in intensity is observed, which confirms the lack of long-range magnetic ordering in the extended temperature range (4–300 K).

2. X-ray photoelectron studies

XPS measurements provide information on the surface composition and therefore we performed Mn- $2p$ and Co- $2p$ core-level XPS to assign the atomic oxidation states of Mn and Co in the SLCMO compound. The spin-orbit splitting of Mn $2p$ peaks corresponds to Mn $2p_{3/2}$ and Mn $2p_{1/2}$, which are located at 641.97 and 653.38 eV, respectively [inset Fig. 3(a)], whereas Co $2p$ peaks [inset Fig. 3(b)] are found at 779.93 eV (Co $2p_{3/2}$) and 795.33 eV (Co $2p_{1/2}$). The oxidation state of Mn/Co ions was determined by the curve fitting the corresponding $2p$ spectral peaks. The experimental peak shape for Mn $2p_{3/2}$ and Co $2p_{3/2}$ was modeled by employing double peak (Gaussian-Lorentzian) patterns and is shown in Figs. 3(a) and 3(b), respectively. Both Mn $2p_{3/2}$ and Co $2p_{3/2}$ spectra show perfect fitting for mixed valence states. The two binding-energy values obtained for Mn $2p_{3/2}$ at 641.17 and 643.87 eV matched well with the reported values for Mn³⁺ and Mn⁴⁺, respectively [28,29]. Similarly, Co $2p_{3/2}$ spectra match with the reported binding-energy values of the 3+ and 2+ state at 779.8 and 780.2 eV, respectively [28,29]. Peak fitting corresponding to Mn $2p_{1/2}$ and Co $2p_{1/2}$ spectra is given in the Supplemental Material [26], which again confirms the mixed valence state. From the XPS fitting, we have estimated the percentage of Mn³⁺/Mn⁴⁺ to be 67/33% and that of Co³⁺/Co²⁺ to be 65/35%. Hence, the predominant oxidation states in SLCMO are confirmed to be Mn³⁺ and Co³⁺, which also corroborates the charge states obtained from the neutron-diffraction data. These observations lend strong support to the counterpart of DFT calculations.

B. Magnetic properties

1. Dc susceptibility

Figure 3(c) shows the temperature dependence of the dc magnetic susceptibilities $\chi(T)$ of SLCMO in the ZFC and

FC conditions under applied fields of 100, 200, and 1000 Oe. The ZFC curve shows two broad peaks (humps) at ~ 150 and ~ 50 K, whereas, the FC curve shows a sharp rise at ~ 140 K followed by an anomaly below ~ 50 K (slope change) at low temperatures. The temperature-dependent derivative curves (dM_{ZFC}/dT) [inset Fig. 3(c)] reveal these two transitions at $T_{C1} \sim 150$ K and $T_{C2} \sim 50$ K. The susceptibility data under an applied field of $H = 100$ Oe (ZFC) in the temperature range 180–300 K were fitted with the Curie-Weiss (CW) law, i.e., $\chi^{-1}(T) = C/(T-\theta_p)$ [Fig. 3(d)], where C and θ_p are Curie constant and CW temperature, respectively. The fit provided positive values of CW constant [$\theta_p = 99$ K] suggesting the presence of dominant ferromagnetic interactions. The effective paramagnetic moment calculated from the Curie constant of $C = 6.42$ emu.K.mol⁻¹ Oe⁻¹ is $\mu_{\text{eff}} = 4.86 \mu_B/\text{f.u.}$ —the theoretically estimated value $4.54 \mu_B \{\mu_{\text{the}} = \sqrt{4S(S+1)}\mu_B\}$ on considering the high-spin (HS) state of Mn³⁺/Mn⁴⁺ [67/33%] and Co³⁺/Co²⁺ [65/35%] from the XPS is taken into account. In general, a strong ferromagnetic compound with long-range magnetic interaction exhibits CW temperature θ_p to be equal to or greater than Curie temperature T_C . However, in disordered systems randomly distributed magnetic ions provide competing magnetic interactions and spin frustrations resulting in $\theta_p < T_C$ [30]. The bifurcation between ZFC and FC arms and the lower-temperature transition at 50 K indicate that there might exist spin-glass (SG) or glassy-like magnetic interaction in addition to the FM interactions, which will be clarified in later sections.

2. Memory effect

The dc thermomagnetic analysis of SLCMO suggests glassy magnetic transition at lower temperatures. Magnetic memory effect is an experimental fingerprint of glassy magnetic material. We have performed the same to figure out the glassy magnetic features in SLCMO. We have carried out a detailed magnetic memory analysis using both ZFC and FC experimental protocols [31]. The ZFC memory experiments were carried out by conventional procedure with cooling the sample without field at a constant rate of 2 K/min

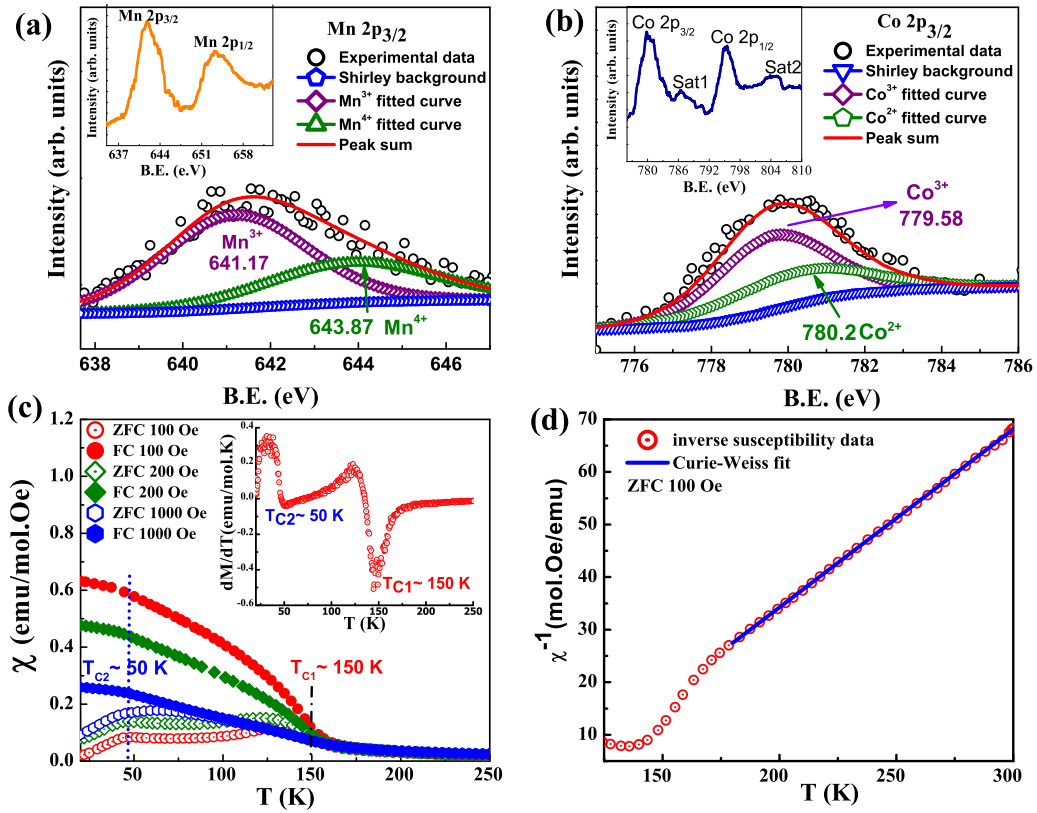


FIG. 3. X-ray photoemission spectroscopy of (a) Mn $2p_{3/2}$ (the inset shows the Mn $2p$ core-level spectrum) and (b) Co $2p_{3/2}$ along with fitted curves (the inset shows the Co $2p$ core-level spectrum). (c) Magnetic susceptibility χ measured under 100, 200, and 1000 Oe with ZFC and FC protocols. The dotted vertical lines indicate two transitions at $T_{C1} = 150$ K and $T_{C2} = 50$ K, respectively [the inset shows the derivative of magnetization vs temperature curve (ZFC) measured under 100 Oe]. (d) The inverse magnetic susceptibility (χ^{-1}) vs temperature curve, for ZFC at 100 Oe.

with an intermediate halt at 40 K for a duration of 1h. The magnetization data with respect to ZFC memory were recorded during the warming cycle without any halt under an applied dc field of 100 Oe. Figure 4(a) depicts the temperature dependence of ZFC reference magnetization M_{ZFCW}^{ref} and ZFC memory magnetization M_{ZFCW}^{mem} along with the differential curve. A sharp memory dip in the differential curve at 40 K shows the clear time evolution of magnetization at the stopping temperature and confirms the glassy dynamics in SLCMO below T_{C2} . For FC memory, first the sample was cooled from 300 to 5 K at a constant rate of 2 K/min under a cooling field of 100 Oe with recurring stops at 100, 40, and 10 K for a duration of 1h at each stop. During each stop the field was set to zero to let the magnetization relax downward. After each stop and wait period [where we see a sharp step during each halted temperature in Fig. 4(b), blue solid line with open diamond symbol with dot], the 100-Oe field is reapplied and cooling is further resumed. This cooling procedure produces sharp jumps in the $M(T)$ curve at the halt temperatures. The data thus obtained are considered as M_{FC}^{stop} . After reaching the base temperature 5 K, the sample temperature is raised continuously at the 2-K/min rate in a constant 100-Oe field and the magnetization is recorded again. This curve is called the M_{FCW}^{mem} curve. Figure 4(b) represents the FC memory plots where the M_{FC}^{stop} curve exhibits sharp jumps at halt temperatures (100, 40, and 10 K) while the M_{FCW}^{mem} curve exhibits two clear upturns near

the stopping temperatures at 10 and 40 K, which is below T_{C2} . However, the M_{FCW}^{mem} curve depicts a continuous curve without any noticeable change at the stopping temperature of 100 K [see Fig. 4(b) solid red line], which is above T_{C2} . Thus, clear magnetic memory effects are observed at temperatures 10 and 40 K confirming that the present compound remembers its previous history of zero field relaxation only below T_{C2} due to the slow dynamics of frozen spins in this region. Hence, it is confirmed from both ZFC and FC memory experiments that the low-temperature transition exhibited by SLCMO at T_{C2} is a glassy magnetic transition and the high-temperature transition at T_{C1} is a ferromagnetic transition.

3. Ac susceptibility

To confirm the true nature of magnetic ordering in this compound, we have measured the temperature-dependent ac susceptibility (χ_{ac}), under an ac field of 2 Oe within the frequency (f) range of 3 to 923 Hz. In agreement with the dc susceptibility data, the temperature dependence of the real part of the ac-susceptibility curves (χ') shows two pronounced peaks at around ~ 150 and 50 K as shown in Fig. 4(c). The frequency variation study reveals that the position of the high-temperature peak (~ 150 K) does not shift, and all the curves at various frequencies merge well above ~ 150 K, confirming paramagnetic to ferromagnetic phase transition at T_{C1} , whereas the peak at ~ 50 K has a pronounced frequency dependence shift; i.e., with increasing frequencies, the peak

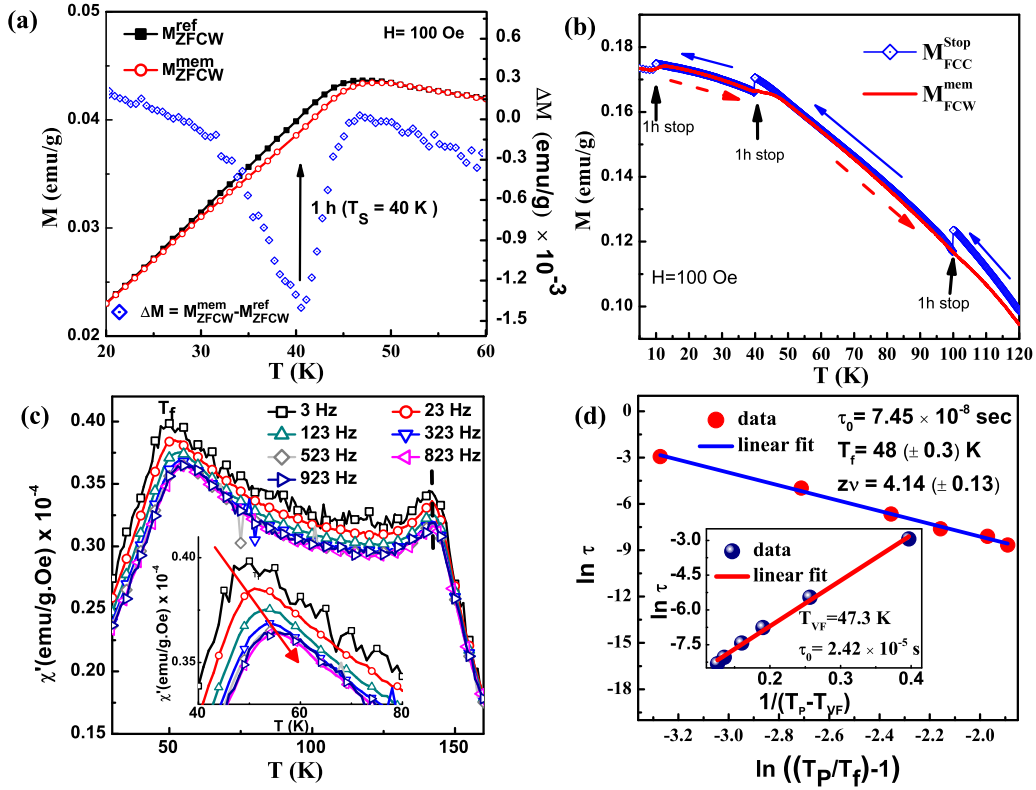


FIG. 4. (a) ZFC memory effect measured after halting for 1 h at 40 K while cooling from 300 to 5 K and then measurement was done in the warming cycle under an applied field of 100 Oe. The difference curve $\Delta M = M_{ZFCW}^{mem} - M_{ZFCW}^{ref}$ is given as a function of temperature. For the reference curve, the sample was cooled to 5 K from 300 K without a halt and measurement was done in the warming cycle. (b) FC memory effect experiment: Intermittent-stop cooling magnetization M_{FCC}^{stop} at 100, 40, and 10 K while cooling from 300 to 5 K (marked as a solid blue arrow) and the red solid line is the continuous warming memory curve M_{FCW}^{mem} (marked as a dashed red arrow). (c) Temperature dependence of the real part of ac susceptibility (χ') measured under different frequencies with ac magnetic field of 2 Oe. The inset shows the plot of $\ln \tau$ vs $\ln \left(\frac{T_P}{T_f} - 1 \right)$ (red solid circles), the best fit to Eq. (2) (solid blue line), and the zoomed portion of T_{C2} . (d) $\ln \tau$ vs $\frac{1}{(T_P - T_{VF})}$ plot for cluster glass transition where the solid line is the linear fit for the Vogel-Fulcher law [Eq. (1)].

shifts towards high temperature from 49.82 K at 3 Hz to 55.25 K at 923 Hz, with a decrease in peak amplitude as shown in the inset of Fig. 4(c). Such behavior is a characteristic feature of the SG and/or disordered magnetic systems [32]. In order to differentiate between the SG and CG behavior, we have carried out the analysis of the susceptibility data at T_{C2} using the Mydosh parameter, Vogel-Fulcher (VF) relation, and slow dynamics models [33]. First, the Mydosh parameter ($K = \frac{\Delta T_P}{T_P \Delta(\log_{10} f)}$), which is empirically known as the relative frequency shift in the peak temperature T_P of χ' per decade of frequency [32], is found to be 0.04 (± 1) and this value is comparable to the values reported for other CG systems ($K \leq 0.08$) [34,35].

Second, we used the VF relation to understand the characteristic relaxation time, which diverges at the freezing temperature T_{VF} :

$$\tau = \tau_0 \exp \frac{-E_a}{k_B (T_P - T_{VF})}, \quad (1)$$

where τ_0 represents the characteristic relaxation time of the clusters, E_a is the activation energy, and T_{VF} is the VF freezing temperature which provides interclusters interaction strength. The expression is valid for peak temperature (T_P) greater than T_{VF} [33]. The linear fitted $\ln \tau$ versus $1/(T_P - T_{VF})$ curve,

obtained by the Souletie and Tholence method [36] with $T_{VF} = 47.3$ K, is shown in the inset of Fig. 4(d). The curve yields $E_a/k_B = 19.65$ (4) K and $\tau_0 = 2.42 \times 10^{-5}$ s, which falls within the range of characteristic relaxation times for CG [35].

Finally, we have fitted experimental data [Fig. 4(d)] by the conventional critical slowing down dynamics model [32]:

$$\tau = \tau^* \left(\frac{T_P - T_f}{T_f} \right)^{-z\nu}, \quad (2)$$

where τ is the relaxation time corresponding to the measured frequency, τ^* is the microscopic relaxation time, $z\nu$ are the dynamic critical exponents, and T_f is the static finite freezing temperature for $f \rightarrow 0$ Hz. We observed that our data well fitted to Eq. (2) as shown in Fig. 4(d); the best fit yields $\tau^* \approx 7.45 \times 10^{-8}$ s and $z\nu \approx 4.14(\pm 0.13)$, with $T_f \approx 48$ K. The critical exponent falls inside the typical range for glassy magnetic systems ($z\nu \sim 4-12$), and observed fitted values are close to those reported for CG ($\tau^* \approx 10^{-8}$ s and $z\nu \approx 6$) [37]. The observed lengthier relaxation time obtained from both VF and critical slowing down relaxation exemplars in conjunction with the calculated Mydosh parameter value confirms the CG behavior of the sample below T_f at 48 K.

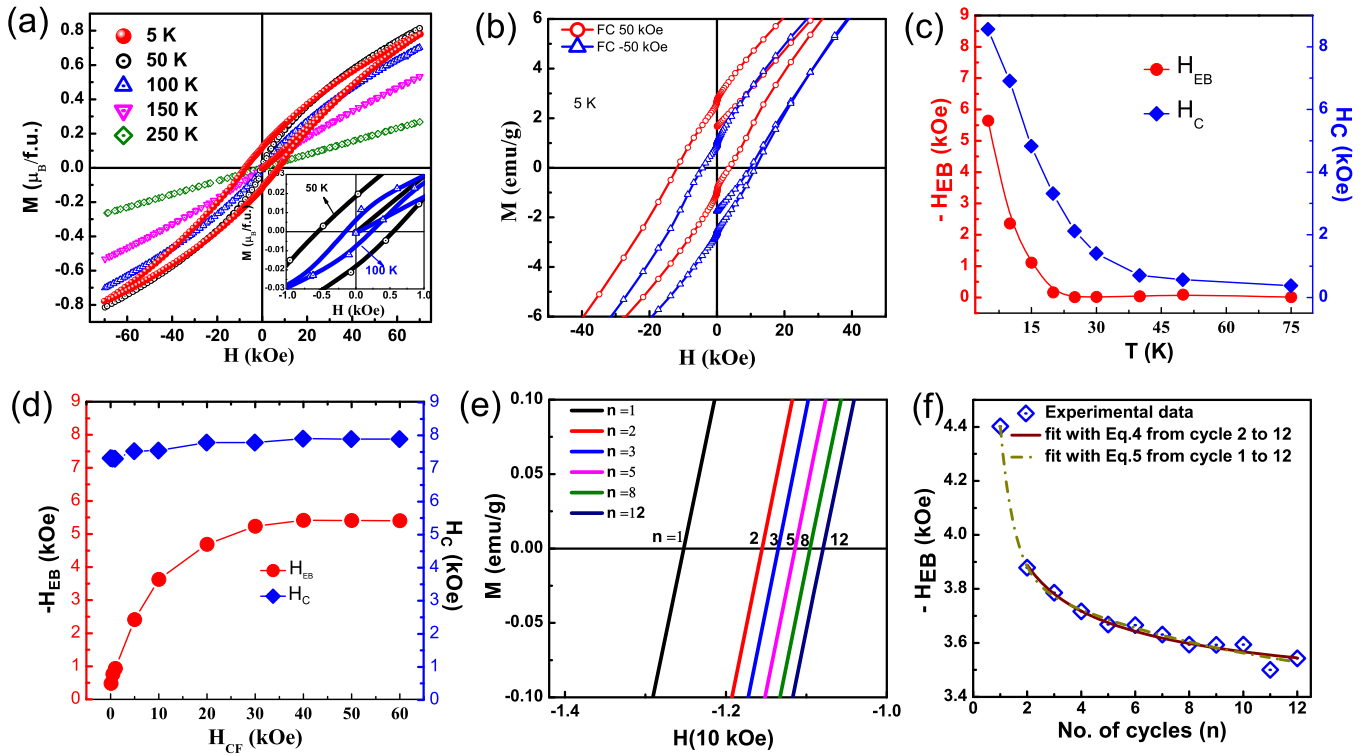


FIG. 5. (a) M - H loops at different temperatures in the range ± 70 kOe (Inset shows the zoom of the interior region in the curve at 50 and 100 K). (b) The M - H hysteresis loops measured at 5 K after cooling the sample from 300 K under 50-kOe field. The measurement range is ± 70 kOe. For clarity, only the data ± 50 kOe are shown. (c) H_{EB} and H_C as a function of cooling fields at 5 K. (d) Temperature-dependent H_{EB} and H_C in cooling field 50 kOe. (e) Magnetization curves measured at 5 K after field cooling ($H_{FC} = 50$ kOe) with 12 continuous loops and a zoom of the left side of the hysteresis curves around $M = 0$; notice the significant difference from $n = 1$ to 2 vs any other consecutive loops. (f) Training effect of FC exchange bias field (H_{EB}) vs amount of hysteresis at 5 K. The curves are fitted by two different conditions.

4. Isothermal magnetization and exchange bias

Figure 5(a) shows the M - H plot for the SLCMO sample measured at 5, 50, 100, 150, and 250 K. The linear isothermal magnetization curve at 250 K indicated the paramagnetic phase of the sample. For $T = 150$ K and below, the M - H curve diverged from the linearity, and the hysteresis loop becomes more prominent below T_{C1} . An enlarged view of hysteresis loops at 50 and 100 K is given in the inset of Fig. 5(a). The absence of long-range ordering between the magnetic cations (which is confirmed from neutron diffractions) along with the presence of frozen spins at lower temperatures confirms the coexistence of ferromagnetic-antiferromagnetic phases in SLCMO. Therefore, the transition below 150 K is a weak ferromagnetic transition resulting with low coercivity below 150 K down to T_{C2} (100 K, $H_C \sim 200$ Oe; 50 K, $H_C \sim 600$ Oe). However, in SLCMO an enhanced coercivity is observed below CG (T_{C2}) transition and it reaches a maximum value of about ~ 7500 Oe at 5 K. As the system enters into the CG region the coercivity is enhanced due to spin freezing phenomena. When the magnetic moments freeze below $T < T_{C2}$, the spins are trapped in the increased free-energy barriers between multiple energy states. So, in an applied field the magnetization direction is flipped, and thus the coercivity is enhanced in order to overcome the increased free-energy barrier [38]. The estimated magnetization measured at 5 K and high field of 70 kOe is $0.8 \mu_B/f.u.$, which is smaller than the expected spin-only saturation magnetization

value of $3.66 \mu_B/f.u.$ (this value is calculated by considering the spin states ratio obtained from XPS with Mn and Co ions as high-spin states). This massive reduction in observed magnetic moments at 5 K strongly implies the presence of competing AF interactions inside the multiple ferromagnetic islands.

Exchange bias is a phenomenon formed due to the magnetic anisotropy created at the interface of AFM and FM phases [39,40]. There are several reports regarding the presence of EB in magnetic oxides with competing magnetic interactions [41–43]. Since the present system possesses different magnetic interactions leading to CG and FM transitions, we have comprehensively investigated the EB effect in SLCMO. The magnetic hysteresis measurements at 5 K were performed in ZFC as well as FC cycles at different values of applied cooling field (CF) and temperatures to understand EB for this system in detail. In FC mode the sample was cooled under a magnetic field of 50 kOe (other than specified) from 300 K to the measurement temperature.

In earlier reports [44,45], it has been noticed that the incorrect optimization of maximum measuring fields can lead to the existence of a minor loop effect. To rule out the minor loop effects and to ensure the observation of a genuine EB shift, we have considered the following point: the anisotropy field (H_A) of the system should be less than the optimal maximum applied field (H_{max}).

Now to obtain the anisotropy field, we have used the law of approach for the saturation magnetization equation on the

initial magnetization virgin curve at 5 K [46], i.e.,

$$M = M_s * \left(1 - \frac{a_1}{H} - \frac{a_2}{H^2}\right) + \chi H, \quad (3)$$

where a_1 and a_2 are the free parameters, M_s is the saturation magnetization, and χ is the high-field susceptibility. According to Andreev *et al.* [46] the first term in Eq. (3) is related to a local anisotropy which originates from the structural defects and nonmagnetic inclusions of local magnetization, while the second term corresponds to the rotation of magnetization against the magnetocrystalline energy. In case of high anisotropic ferromagnet compounds $a_1 \ll a_2$ ($a_2 = \frac{4K_1^2}{15M_s^2}$), where constant a_2 provides the estimation of magnetocrystalline anisotropy.

A rough estimation of the anisotropy field $H_A = \frac{2K_1}{M_s}$ was obtained by using Eq. (3) (where K_1 is an anisotropy constant). From 5-K M - H data, the anisotropy field of ~ 20 kOe was obtained by using Eq. (3), which is comparable to the value reported for Fe-doped LaMnO₃ [47]. The values of H_{\max} were considered much higher than $H_A \sim 20$ kOe for the major hysteresis loop tracing. Additionally, to rule out the minor loop presence, we have recorded the hysteresis loop under positive and negative CF of 50 kOe. The hysteresis loops are found to be shifted towards the opposite direction to the applied CF, which is a signature of conventional EB presence in this compound [Fig. 5(b) shows zoomed versions of the hysteresis loops at ± 50 kOe for the sake of clarity].

Traditionally, EB and coercivity values are obtained as $H_{\text{EB}} = \frac{(H_{c1} + H_{c2})}{2}$ and $H_C = \frac{(|H_{c1}| + |H_{c2}|)}{2}$, where H_{c1} and H_{c2} are left and right coercive fields, respectively. The hysteresis curves in a cooling field of 50 kOe measured at different temperatures from 5 to 75 K in the field range ± 70 kOe and the values of H_{EB} and H_C are plotted as a function of temperatures [Fig. 5(c)]. The H_{EB} versus temperature curve shows an exponential decay behavior. One can see that the EB appears below $T_f = 48$ K of the CG state. At 5 K, the displacement of the FC loop becomes much more prominent with $H_{\text{EB}} = 5.5$ kOe at a CF of 50 kOe, which is ten times larger than that of the double perovskite compound LaSrCoMnO₆ involving same magnetic ions (measured in the same condition, i.e., at 5 K with CF 50 kOe) [23]. Also, we have performed the cooling field from 0.01 to 60 kOe dependence of the EB [Fig. 5(d)] at 5 K with a maximum field range of 70 kOe. We observe a sharp increase in both H_{EB} and H_c with increasing CF up to 40 kOe with a giant EB of ~ 5.5 kOe followed by a more gradual saturation of this effect at higher CFs up to 60 kOe. When cooling the specimen to $T < T_f$, in the presence of a magnetic field, the CG spins next to the FM/AFM spins arrange along a specific direction due to the exchange interaction at the frustrating interface. As a result, there will be strong pinning between frozen FM and AFM islands of spin clusters and the FM spins producing EB effect along the CF direction.

Training effects are complementary characteristics of EB phenomena and occurring by the nonequilibrium nature of the spin structures in the pinning layer [48]. While cycling the system through several consecutive hysteresis loops, it is manifested as the gradual decrease in H_{EB} and shows a clear indication of rearrangements in the pinning layer spin structure towards an equilibrium configuration supporting Binek's

proposition on EB effect in antiferromagnetic-ferromagnetic heterostructures. Later Mishra *et al.* [49] proposed that local spins of the AFM side of the interface are affected by the components of both frozen and rotating spins by the FM magnetization reversal. In this view, a series of 12 continuous hysteresis loops were measured at 5 K over ± 70 kOe under a CF of 50 kOe as shown in Fig. 5(e), which illustrates a close view of the left side of hysteresis curves around the $M = 0$ axis. The H_{EB} values obtained from each $M(H)$ are plotted with the number of hysteresis cycles (n) in Fig. 5(f). A monotonic decrease of the EB effect is observed with continuous loops measurement. The following power-law function can describe the reduction of H_{EB} as a function of n in terms of energy dissipation of the AFM regions at the pinning interfaces:

$$H_{\text{EB}} - H_{\text{EB}}^{\infty} \propto n^{-\frac{1}{2}}, \quad (4)$$

where n is the loop index number and H_{EB}^{∞} is the value at $n = \infty$ which is 3.188 kOe for the present sample. Equation (4) holds only for loops from $n \geq 2$, and cannot explain the shear relaxation between the first and second loops as shown in Fig. 5(f). According to Mishra *et al.*, interfacial spin frustration can occur at the magnetically disordered FM/AFM interface due to AFM magnetic anisotropy. This magnetic anisotropy is contributed from two different types of AFM spins after field cooling: specifically, frozen and rotatable AFM spins [49]. As this compound exhibits EB below the CG transitions with disordered FM/AFM phases, it is appropriate to use the model [Eq. (5)] proposed by them for fitting the training effect. The equation which satisfies the condition is expressed as

$$H_{\text{EB}}^n = H_{\text{EB}}^{\infty} + A_f \left(\frac{-n}{P_f}\right) + A_r \left(\frac{-n}{P_r}\right), \quad (5)$$

where f and r denote the frozen and rotatable AFM spin components at the pinning interface. The parameters A have dimensions of magnetic field (Oe), whereas parameters P are dimensionless quantities identified with relaxation. As can be seen from Fig. 5(f), the FC EB training effect data fit well with Eq. (5) in comparison to Eq. (4). The parameters obtained from the fit to the H_{EB} data are $H_{\text{EB}}^{\infty} = 3.4$ kOe, $A_f = 3.8$ kOe, $P_f = 0.51$, $A_r = 0.505$ kOe, and $P_r = 8.71$, which suggest that the rotatable components are relaxed 17 times faster than the frozen spin component at the interface in the presence of cooling field of 50 kOe. Similar phenomena have been observed in a spin-glass system of La_{1.5}Ca_{0.5}CoIrO₆ [41].

IV. ESTIMATION OF EXCHANGE BIAS FROM DFT CALCULATIONS

The experimental results conclusively show the CG magnetic structure and a giant exchange bias for SLCMO RP structure. The CG state of the system suggests coexistence of AFM- and FM-rich domains and the EB occurs at the boundary between these domains. Experimentally it has been reported that Sr_{2-x}La_xCo/MnO₄ has a rich magnetic phase diagram depending on the La and Sr concentration [50–54]. Our electronic structure calculations along with the reported literature confirm that pristine LaSrCoO₄ and LaSrMnO₄ have

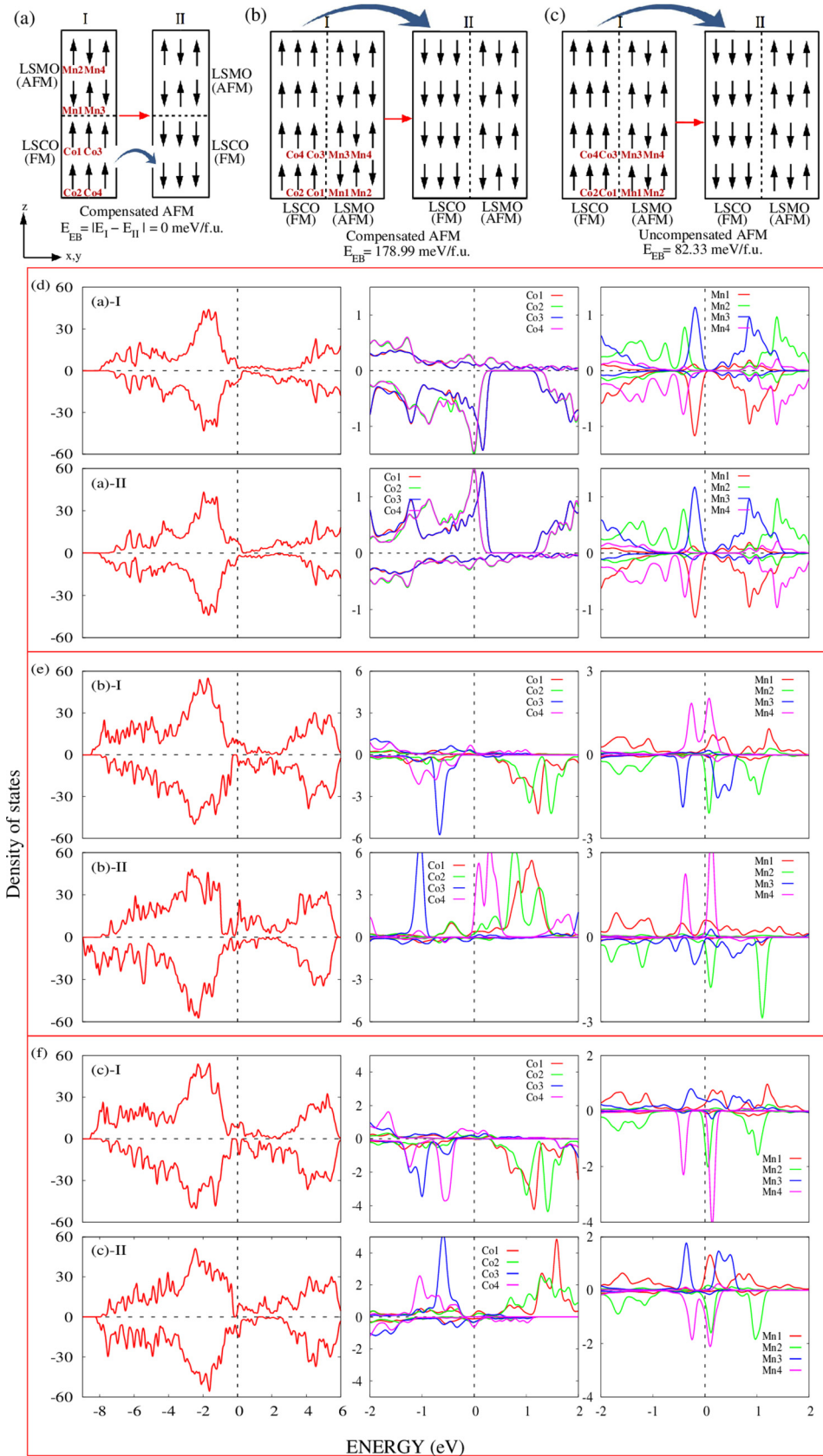


FIG. 6. Schematics for three different possible interfaces between FM LaSrCoO_4 (LSCO) and AFM LaSrMnO_4 (LSMO) to study the exchange bias effect in the $\text{SrLaCo}_{0.5}\text{Mn}_{0.5}\text{O}_4$ compound. The dotted lines represent the interface. (a) LSCO and LSMO are repeated along the z axis, (b, c) Interface with compensated and uncompensated AFM at the interface layers, respectively, in which LSCO and LSMO are repeated along x or y axes to make the supercell. The exchange bias energy (EB) for each case is calculated by the spin-flip mechanism of the Co atoms in the FM LSCO layers. The spin flips for Co atoms for each case are represented using the blue arrows. The results are obtained from DFT+ U calculations with $U = 5$ eV. (d) For interface (a), (a-I) and (a-II) show the total and partial densities of states (DOS) before and after spin flip, respectively. Similarly, (b-I, b-II) and (c-I, c-II) show the total and partial DOS for interfaces (b) and (c), respectively.

FM [55] and AFM [50,56–59] states, respectively. However, LaSrCoO_4 is also reported as a spin glass in a recent paper [60]. The earlier discussions on the magnetic measurements have revealed the coexistence of both AFM and FM phases

at low temperature (<50 K). Further, short-range magnetic ordering is inferred from the combined study of neutron diffraction, dc and ac susceptibility measurements. However, the XRPD/NPD do not indicate any Co- and Mn-rich segre-

gated phases. Therefore, the coexistence of the FM and AFM ordering can be explained provided there are subnanoscale (two to three unit-cell length) Co- and Mn-rich domains. The primary arrangements of such FM and AFM domains are shown in Fig. 6. The secondary arrangements can be obtained through vector combination of these primary arrangements. Using DFT calculations, the strength of exchange bias is estimated by spin-flipping mechanism [61].

Under the collinear arrangement and the spin-flip mechanism, the EB is calculated as follows. In each of the supercells, the spin of the Co atoms in the FM LSCO layers is flipped, whereas that of Mn atoms in AFM LSMO layers remains the same. The exchange bias energy (E_{EB}) is the difference ($|E_I - E_{II}|$) between the two cases, i.e., between the spin-up (E_I) and spin-down (E_{II}) arrangement for Co atoms in the FM LSCO layer. A similar method was also adopted earlier to study the exchange bias effect in SrRuO₃/SrMnO₃ [61]. In the first case [Fig. 6(a)], the EB is zero, suggesting weak magnetic coupling among the Co and Mn layers of atoms along the z axis. This is due to the large layer separation of 6.31 Å.

In the second case, two possible types of interfaces are considered depending on the spin alignment of the Mn atoms [Figs. 6(b) and 6(c)]. In these two types of interfaces, the spin alignment of the Mn atom at the interface layer is different. In the first case [Fig. 6(b)], the Mn spins at the interface layer are opposite to each other to form a compensated AFM structure. In the second structure [Fig. 6(c)], the spin alignment of the Mn atoms in the interface layer is in the same direction to produce uncompensated moments at the interface. In case of the supercells having compensated and uncompensated LSMO AFM layers at the interface, the EBs are found to be 178.99 and 82.33 meV/f.u., respectively. The Mn-Co distance in such supercells is 3.84 Å. The compensated AFM layer at the interface, in principle, should not show any exchange bias effect [39]. However, in our calculation, for such an interface, we found there is a significant value of the exchange bias energy.

Origin of exchange bias

To explain the origin of the exchange bias energy, we shall consider the difference between the magnetic interaction energy (J_{ij}), given by the Hamiltonian:

$$H = - \sum_{i,j} J_{ij} \vec{S}_i \cdot \vec{S}_j . \quad (6)$$

First, we consider the case of the uncompensated LSMO AFM at the interface layer [Fig. 6(c)] with configuration I. The total magnetic interaction energy (J_{tot}) for this configuration is $8J_1 - 8J_2 + 8J_3$, where J_1 , J_2 , and J_3 are the interaction energies between Co-Co, Mn-Mn, and Co-Mn, respectively. The interaction is considered positive for the same spin, whereas it is considered to be negative for AFM ordering between two atoms. Similarly, for configuration II, the total magnetic exchange interaction energy is $8J_1 - 8J_2 - 8J_3$. Therefore, the difference in magnetic energy between the two systems is $16J_3$, which further leads to exchange bias energy.

To further analyze, in the lower panels of Fig. 6, we have plotted the total and Mn/Co- d density of states (DOS) before and after spin flip for the aforementioned interfaces. From the total DOS for each of these interfaces, we observe finite DOS at E_F in either of the spin channels, suggesting the FM metallic behavior. From the partial DOS plots, we find that Mn- d states create a (pseudo) gap at E_F , which is similar to the pure AFM and insulating LSMO bulk compounds [56], whereas the Co- d states cross the E_F , which is the case for the intermediate spin state as observed earlier in the FM and metallic LSCO compound [55]. This further confirms that the bulk magnetic phases are nearly maintained. Minor deviations are due to coupling between the Mn and Co spins across the interface.

For the interface along [001], we find that the DOS does not change with spin flipping. This is because the strength of the magnetic coupling across the interface remained unaltered, leading to the absence of an exchange bias effect for this interface. However, for the interface along x and y , the DOS at E_F changes significantly with spin flipping, suggesting a variation in the magnetic coupling. Therefore, the total energy of these configurations with spin flipping changes to create an exchange bias effect.

V. CONCLUSIONS

To summarize and conclude we have carried out a combined experimental and theoretical investigation to show that SLCMO produces an exchange bias as large as 5.5 kOe. To our understanding, this is the highest ever reported among all the transition-metal layered oxides. The glassy magnetic nature of the sample has been confirmed using ac and dc magnetic measurements. As the first-principles electronic calculations suggest, the origin of this glassy phase and, subsequently, the exchange bias effect is ascribed to the presence of competing magnetic interaction at the interface between magnetic domains at the subnanoscale. This paper concludes that new layered oxides with more than one transition metal can be designed to create natural/artificial magnetic interfaces so that tunable giant exchange bias can be observed at the desired temperature.

ACKNOWLEDGMENTS

P.N.S. acknowledges the Council of Scientific and Industrial Research, India for financial support (Project No. 03 (1214)/12/EMR-II). We acknowledge Nano Functional Materials Technology Centre of Indian Institute of Technology Madras for X-ray Photoelectron spectroscopy measurement. We wish to thank Dr. A. Senyshyn for his help in the neutron diffraction experiment. The author T.C. gratefully acknowledges the financial support provided by FRM II to perform neutron scattering experiments at the Heinz Maier-Liebnitz Zentrum (MLZ), Garching, Germany. The theoretical part of this work is supported by DST, India through Grant No. EMR/2016/003791. P.P. and B.R.K.N. would like to acknowledge the High Performance Computing

Environment facility of Indian Institute of Technology Madras. P.P. acknowledges Indian Institute of Technology Madras for the Institute Postdoctoral fellowship. R.R.D. is

grateful to Dr. P. Neenu Lekshmi for many fruitful discussions. R.R.D. thanks Indian Institute of Technology Madras Alumni for the travel support.

- [1] S. Baidya and T. Saha-Dasgupta, *Phys. Rev. B* **84**, 035131 (2011).
- [2] J. Su, Z. Z. Yang, X. M. Lu, J. T. Zhang, L. Gu, C. J. Lu, Q. C. Li, J. M. Liu, and J. S. Zhu, *ACS Appl. Mater. Interfaces* **7**, 13260 (2015).
- [3] S. Yáñez-Vilar *et al.*, *Phys. Rev. B* **84**, 134427 (2011).
- [4] N. Lee, H. Y. Choi, Y. J. Jo, M. S. Seo, S. Y. Park, and Y. J. Choi, *Appl. Phys. Lett.* **104**, 112907 (2014).
- [5] R. von Helmolt, J. Wecker, B. Holzapfel, L. Schultz, and K. Samwer, *Phys. Rev. Lett.* **71**, 2331 (1993).
- [6] S. Jin, T. H. Tiefel, M. McCormack, R. A. Fastnacht, R. Ramesh, and L. H. Chen, *Science* **264**, 413 (1994).
- [7] Y. Tokura, *Rep. Prog. Phys.* **69**, 797 (2006).
- [8] D. G. Schlom, L.-Q. Chen, X. Pan, A. Schmehl, and M. A. Zurbuchen, *J. Am. Ceram. Soc.* **91**, 2429 (2008).
- [9] H. Y. Hwang, Y. Iwasa, M. Kawasaki, B. Keimer, N. Nagaosa, and Y. Tokura, *Nat. Mater.* **11**, 103 (2012).
- [10] J. Chakhalian, A. J. Millis, and J. Rondinelli, *Nat. Mater.* **11**, 92 (2012).
- [11] S. N. Ruddlesden and P. Popper, *Acta Crystallogr.* **10**, 538 (1957).
- [12] J. B. Torrance, Y. Tokura, A. I. Nazzari, A. Bezinge, T. C. Huang, and S. S. P. Parkin, *Phys. Rev. Lett.* **61**, 1127 (1988).
- [13] R. J. Cava, R. B. van Dover, B. Batlogg, and E. A. Rietman, *Phys. Rev. Lett.* **58**, 408 (1987).
- [14] S. B. Wilkins, P. D. Spencer, P. D. Hatton, S. P. Collins, M. D. Roper, D. Prabhakaran, and A. T. Boothroyd, *Phys. Rev. Lett.* **91**, 167205 (2003).
- [15] T. Birol, N. A. Benedek, and C. J. Fennie, *Phys. Rev. Lett.* **107**, 257602 (2011).
- [16] P. D. Battle *et al.*, *J. Phys.: Condens. Matter* **8**, L427 (1996).
- [17] M. Lu, X. Deng, J. C. Waerenborgh, X. Wu, and J. Meng, *Dalton Trans.* **41**, 11507 (2012).
- [18] F. Tonus, C. Greaves, H. El Shinawi, T. Hansen, O. Hernandez, P. D. Battle, and M. Bahout, *J. Mater. Chem.* **21**, 7111 (2011).
- [19] C. J. Zhang and H. Oyanagi, *Phys. Rev. B* **79**, 064521 (2009).
- [20] R. Ang, Y. P. Sun, X. Luo, C. Y. Hao, X. B. Zhu, and W. H. Song, *J. Appl. Phys.* **104**, 023914 (2008).
- [21] T. Chakraborty, C. Meneghini, A. Nag, and S. Ray, *J. Mater. Chem. C* **3**, 8127 (2015).
- [22] L. Xie and H. G. Zhang, *J. Appl. Phys.* **113**, 204506 (2013).
- [23] R. C. Sahoo, S. K. Giri, P. Dasgupta, A. Poddar, and T. K. Nath, *J. Alloys Compd.* **658**, 1003 (2016).
- [24] M. Y. Lin, Y. F. Wang, D. C. Ling, H. S. Sheu, and H. C. I. Kao, *J. Supercond. Novel Magn.* **23**, 721 (2010).
- [25] P. Giannozzi *et al.*, *J. Phys.: Condens. Matter* **21**, 395502 (2009).
- [26] See Supplemental Material at <http://link.aps.org/supplemental/10.1103/PhysRevB.98.184417> for further Rietveld refinement details of the x-ray and neutron diffraction study of SLCMO. Also included are X-ray photoemission spectroscopy $2p_{1/2}$ data and the fit procedures used and the corresponding figures.
- [27] A. Cammarata and J. M. Rondinelli, *Phys. Rev. B* **92**, 014102 (2015).
- [28] M. C. Biesinger, B. P. Payne, A. P. Grosvenor, L. W. M. Lau, A. R. Gerson, and R. S. C. Smart, *Appl. Surf. Sci.* **257**, 2717 (2011).
- [29] R. C. Sahoo, D. Paladhi, P. Dasgupta, A. Poddar, R. Singh, A. Das, and T. K. Nath, *J. Magn. Magn. Mater.* **428**, 86 (2017).
- [30] C. L. Bull, H. Y. Playford, K. S. Knight, G. B. G. Stenning, and M. G. Tucker, *Phys. Rev. B* **94**, 014102 (2016).
- [31] Y. Sun, M. B. Salamon, K. Garnier, and R. S. Averback, *Phys. Rev. Lett.* **91**, 167206 (2003).
- [32] J. A. Mydosh, *Rep. Prog. Phys.* **78**, 052501 (2015).
- [33] J. A. Mydosh, *Spin Glasses: An Experimental Introduction* (Taylor & Francis, London, 1993).
- [34] F. Wang, J. Zhang, Y.-f. Chen, G.-j. Wang, J.-r. Sun, S.-y. Zhang, and B.-g. Shen, *Phys. Rev. B* **69**, 094424 (2004).
- [35] V. K. Anand, D. T. Adroja, and A. D. Hillier, *Phys. Rev. B* **85**, 014418 (2012).
- [36] J. Souletie and J. L. Tholence, *Phys. Rev. B* **32**, 516 (1985).
- [37] S. Sabyasachi, M. Patra, S. Majumdar, S. Giri, S. Das, V. S. Amaral, O. Iglesias, W. Borghols, and T. Chatterji, *Phys. Rev. B* **86**, 104416 (2012).
- [38] A. D. Christianson, M. D. Lumsden, M. Angst, Z. Yamani, W. Tian, R. Jin, E. A. Payzant, S. E. Nagler, B. C. Sales, and D. Mandrus, *Phys. Rev. Lett.* **100**, 107601 (2008).
- [39] J. Nogués and I. K. Schuller, *J. Magn. Magn. Mater.* **192**, 203 (1999).
- [40] M.-H. Phan, J. Alonso, H. Khurshid, P. Lampen-Kelley, S. Chandra, K. S. Repa, Z. Nemati, R. Das, Ó. Iglesias, and H. Srikanth, *Nanomaterials* **6**, 221 (2016).
- [41] L. T. Coutrim *et al.*, *Phys. Rev. B* **93**, 174406 (2016).
- [42] S. K. Giri, R. C. Sahoo, P. Dasgupta, A. Poddar, and T. K. Nath, *J. Phys. D* **49**, 165002 (2016).
- [43] Y.-k. Tang, Y. Sun, and Z.-h. Cheng, *Phys. Rev. B* **73**, 174419 (2006).
- [44] L. Klein, *Appl. Phys. Lett.* **89**, 036101 (2006).
- [45] J. Geshev, *J. Magn. Magn. Mater.* **320**, 600 (2008).
- [46] M. I. B. S. V. Andreev, V. I. Pushkarsky, V. N. Maltsev, L. A. Pamyatnykha, N. V. K. E. N. Tarasov, and T. Goto, *Journal of Alloys and Compounds* **260**, 196 (1997).
- [47] M. Patra, M. Thakur, K. De, S. Majumdar, and S. Giri, *J. Phys.: Condens. Matter* **21**, 078002 (2009).
- [48] C. Binek, *Phys. Rev. B* **70**, 014421 (2004).
- [49] S. K. Mishra, F. Radu, H. A. Durr, and W. Eberhardt, *Phys. Rev. Lett.* **102**, 177208 (2009).
- [50] D. Senff, P. Reutler, M. Braden, O. Friedt, D. Bruns, A. Cousson, F. Bourée, M. Merz, B. Büchner, and A. Revcolevschi, *Phys. Rev. B* **71**, 024425 (2005).
- [51] M. Merz, G. Roth, P. Reutler, B. Büchner, D. Arena, J. Dvorak, Y. U. Idzerda, S. Tokumitsu, and S. Schuppler, *Phys. Rev. B* **74**, 184414 (2006).
- [52] J. Herrero-Martín, J. García, G. Subías, J. Blasco, and M. C. Sánchez, *Phys. Rev. B* **72**, 085106 (2005).

- [53] M. Cwik, M. Benomar, T. Finger, Y. Sidis, D. Senff, M. Reuther, T. Lorenz, and M. Braden, *Phys. Rev. Lett.* **102**, 057201 (2009).
- [54] A. V. Chichev *et al.*, *Phys. Rev. B* **74**, 134414 (2006).
- [55] H. Wu, *Phys. Rev. B* **81**, 115127 (2010).
- [56] K. T. Park, *J. Phys.: Condens. Matter* **13**, 9231 (2001).
- [57] C. Baumann, G. Allodi, A. Amato, B. Büchner, D. Cattani, R. De Renzi, R. Klingeler, P. Reutler, and A. Revcolevschi, *Physica B: Condensed Matter* **374–375**, 83 (2006).
- [58] C. Baumann, G. Allodi, B. Büchner, R. De Renzi, P. Reutler, and A. Revcolevschi, *Physica B: Condensed Matter* **326**, 505 (2003).
- [59] S. Larochelle, A. Mehta, L. Lu, P. K. Mang, O. P. Vajk, N. Kaneko, J. W. Lynn, L. Zhou, and M. Greven, *Phys. Rev. B* **71**, 024435 (2005).
- [60] H. Guo, Z. Hu, T.-W. Pi, H. L. Tjeng, and C. A. Komarek, *Crystals* **6**, 98 (2016).
- [61] S. Dong, Q. Zhang, S. Yunoki, J. M. Liu, and E. Dagotto, *Phys. Rev. B* **84**, 224437 (2011).